Magnetic ordering and magnetoelectric coupling in a ferro-rotational frustrated magnet

Junjie Yang [1,*] Shengzhi Zhang [2] Dimuthu Obeysekera [1] Minseong Lee [2] Keith Taddei [3,4] and Prabha Yapa [1]

[1]*Department of Physics, New Jersey Institute of Technology, Newark, New Jersey 07102, USA*

[2]*National High Magnetic Field Laboratory, Los Alamos National Laboratory, Los Alamos, New Mexico 87545, USA*

[3]*Neutron Scattering Division, Oak Ridge National Laboratory, Oak Ridge, Tennessee 37831, USA*

[4]*Advanced Photon Source, Argonne National Laboratory, Lemont, Illinois 40439, USA*

(Received 17 May 2025; accepted 6 October 2025; published 12 November 2025)

Magnetic frustration can suppress conventional magnetic ordering and give rise to exotic magnetic states and emergent functionalities. In this study, we investigate the ferrorotational compound $RbFe(SeO_4)_2$ with strong magnetic frustration. Our results reveal a helical magnetic structure emerging below the Néel temperature $T_N \sim 1.57$ K. Magnetic diffuse scattering above T_N confirms short-range correlations. Magnetoelectric measurements demonstrate magnetoelectric coupling behavior below T_N. Monte Carlo simulations reproduce the experimental χ-T and M-H curves and help extract effective exchange interactions. These findings position $RbFe(SeO_4)_2$ as a promising platform for studying the interplay between spin magnitude, dimensionality, frustration, magnetoelectric coupling, and exploring the crossover between classical and quantum magnetic regimes.

DOI: 10.1103/wjq7-tlk7

I. INTRODUCTION

Magnetic frustration can suppress magnetic ordering and give rise to exotic, coherently disordered magnetic states such as the quantum spin liquid, spin jam, and spin-ice phases [1–6]. It can also lead to a variety of novel noncollinear magnetic structures, including cycloidal spin order, helical spin order, and topological skyrmions [7–13]. These noncollinear spin configurations can further couple with the lattice, resulting in emergent-material functionalities such as magnetoelectric coupling and multiferroicity [12,14–16]. Among various frustrated magnetic systems, triangular-lattice antiferromagnets have remained a long-standing and intensely studied topic of research. For example, two-dimensional (2D) triangular-layered $YbMgGaO_4$ has been proposed as a candidate for realizing quantum spin-liquid states, showing no magnetic order down to temperatures as low as 30 mK [17–19]. 2D triangular-layered compounds of the form $AFe(XO_4)_2$ (A = Rb, Cs; X = Mo, S, Se) exhibit frustration-induced chiral helical magnetic ordering below 4 K [10,11,13–16,20–23]. This magnetic order interacts with structural ferrorotation, leading to magnetoelectric coupling and multiferroic behavior [20,21]. Among the $AFe(XO_4)_2$ family, $RbFe(SeO_4)_2$ remains relatively unexplored, and its magnetic ground state is entirely unknown. It is unclear if this material remains magnetically disordered down to ultralow temperatures or whether it develops helical magnetic order and exhibits magnetoelectric coupling and multiferroicity, as seen in its analogs, e.g., $RbFe(SO_4)_2$ [20,21].

In this work, we report magnetic susceptibility, magnetization, neutron powder diffraction, and magnetoelectric studies of $RbFe(SeO_4)_2$. Magnetic susceptibility measurements as a function of temperature (χ-T) indicate that the magnetic moments in $RbFe(SeO_4)_2$ remain disordered above 1.57 K. The inverse susceptibility ($1/\chi$-T) follows Curie-Weiss behavior with a Curie-Weiss temperature (θ_{CW}) of −9.21 K, which is approximately six times higher than the magnetic ordering temperature ($T_N \sim 1.57$ K), suggesting strong magnetic frustration in this material. Neutron powder diffraction confirms that the crystal structure is ferrorotational at 20 K and that a helical magnetic structure develops below 1.57 K. Above the magnetic ordering temperature, magnetic diffuse scattering is observed, indicating the presence of short-range magnetic correlations and supporting the presence of strong frustration. Magnetoelectric current measurements as a function of the magnetic field reveal magnetoelectric coupling below T_N. Furthermore, Monte Carlo simulations successfully reproduce the experimental magnetization-field (M-H) curves, susceptibility (χ-T) behavior, and the magnetic propagation vector of the helical structure, enabling us to extract possible exchange-coupling constants for $RbFe(SeO_4)_2$. The strong magnetic frustration and low ordering temperature make $RbFe(SeO_4)_2$ a promising platform for future studies aimed at understanding how spin magnitude, dimensionality, and magnetic frustration influence the crossover between classical and quantum magnetic regimes.

II. RESULTS AND DISCUSSIONS

The $RbFe(SeO_4)_2$ single crystals were grown using the hydrothermal method in a 50-ml Teflon-lined autoclave at 483 K [20,21]. The resulting crystals exhibit a hexagonal-plate shape with a yellowish color. First, we measured the χ-T curve of $RbFe(SeO_4)_2$ crystals using a vibrating sample magnetometer over a temperature range of 2 to 300 K. During the measure-

*Contact author: jyang@njit.edu

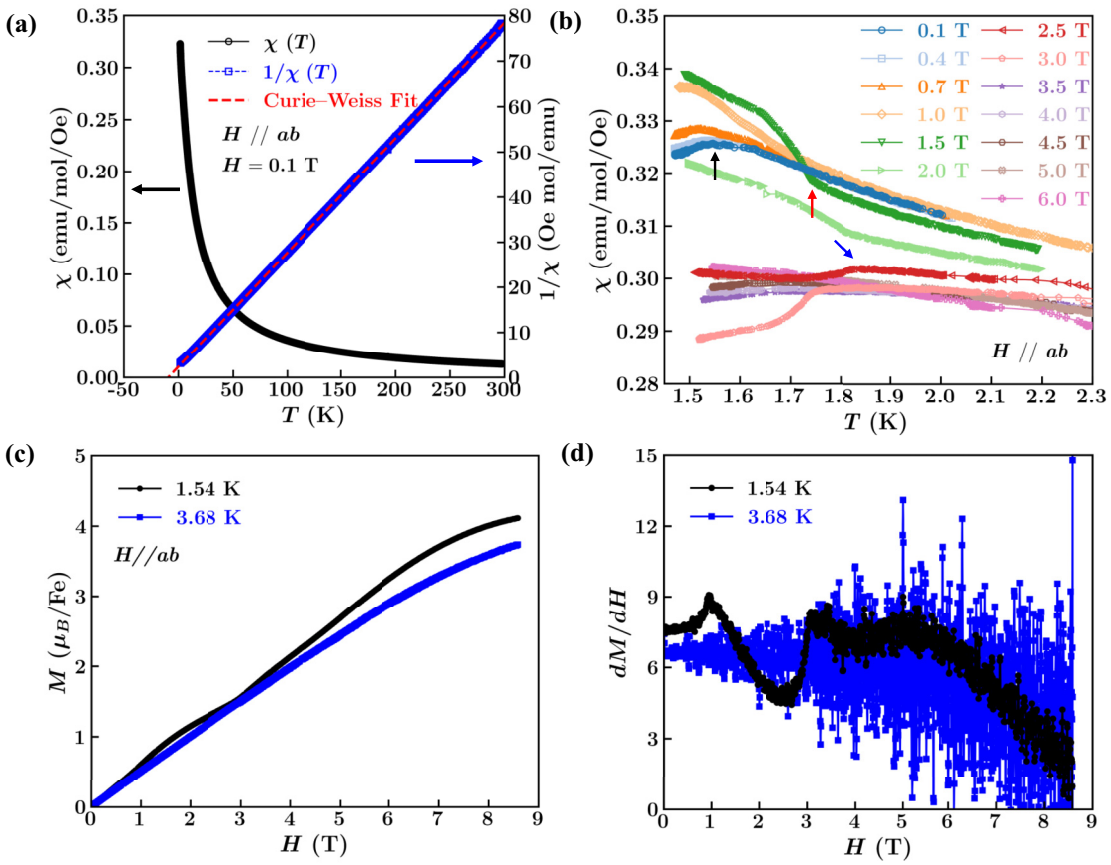

FIG. 1. (a) Temperature dependence of the magnetic susceptibility χ (black) and the inverse magnetic susceptibility $1/\chi$ (blue). The dashed red line represents the Curie-Weiss fit to the $1/\chi$ curve. A 0.1 T magnetic field was applied during the measurement. (b) χ-T curves measured at various magnetic fields in the low-temperature range. The arrows indicate the magnetic transitions. (c) M-H curves measured above (blue) and below (black) the magnetic ordering temperature. (d) Corresponding dM/dH curves calculated from the M-H data. For all measurements shown in panels (a)–(d), the magnetic field was applied along the ab plane of the $RbFe(SeO_4)_2$ crystals.

ments, a magnetic field of 0.1 T was applied along the ab plane of the crystals. As shown on the left axis of Fig. 1(a), the χ-T curve (black) exhibits paramagnetic behavior from 2 to 300 K, with no indication of magnetic transitions. The inverse susceptibility ($1/\chi$) (blue) as a function of temperature is shown on the right axis of Fig. 1(a). We fitted the $1/\chi$-T curve using the Curie-Weiss law $1/\chi = (T - \theta_{CW})/C$. From this fit, we determined the Curie-Weiss temperature $\theta_{CW} \sim -9.21$ K and Curie-Weiss constant $C = 3.945$ emu/mol/Oe/K. The Curie-Weiss temperature can be further analyzed to determine J, the effective intralayer exchange-coupling constant, using the equation $\theta_{CW} = -zJS(S+1)/3$. In this equation, $S = 5/2$ for Fe^{3+} ions, and $z = 6$ represents the number of nearest neighbors. With $\theta_{CW} = -9.21$ K, we calculate $J = 0.526$ K ($\sim$0.045 meV) for our sample. The Curie-Weiss constant can be further analyzed to determine μ_{eff}, the effective magnetic moment of Fe^{3+} ions, using the equation $\mu_{eff} = 2.828\sqrt{C}$. With $C = 3.945$ emu/mol/Oe/K, we calculate $\mu_{eff} = 5.617\,\mu_B$, which is close to the theoretical value for Fe^{3+} ions.

To investigate whether $RbFe(SeO_4)_2$ exhibits magnetic order and how this order evolves under external magnetic fields, we measured the χ-T curves from 1.45 to 2.3 K under various magnetic fields applied along the ab plane. As shown in Fig. 1(b), at a magnetic field of 0.1 T, a peak appears in the χ-T curve near $T_N = 1.57$ K (indicated by the black arrow), suggesting an antiferromagnetic transition. As the magnetic field increases, T_N shifts to lower temperatures and becomes undetectable at 1 T within the temperature range. As T_N is suppressed, a second transition emerges at a higher temperature of $\sim$1.75 K (indicated by the red arrow), which shows a slight increase from 1.5 to 2 T. Upon further increasing the magnetic field, this second transition disappears, and a third type of transition emerges at 1.82 K under 2.5 T (indicated by the blue arrow). With the continued increase in magnetic field strength, this third transition is also gradually suppressed and becomes unobservable at 5 T within the measured temperature window.

Our χ-T results suggest that $RbFe(SeO_4)_2$ exhibits several distinct magnetic states that evolve under external magnetic fields. To further confirm the field-induced magnetic transitions, we measured the M-H curves from 0 to 8.5 T at two temperatures—above and below the T_N—with the magnetic field applied along the ab plane, as shown in Fig. 1(c). At 1.54 K, a 1/3 magnetization plateau is observed between 1 and 3.2 T in the M-H curve. This transition is more clearly identified in the first derivative, dM/dH, shown in Fig. 1(d),

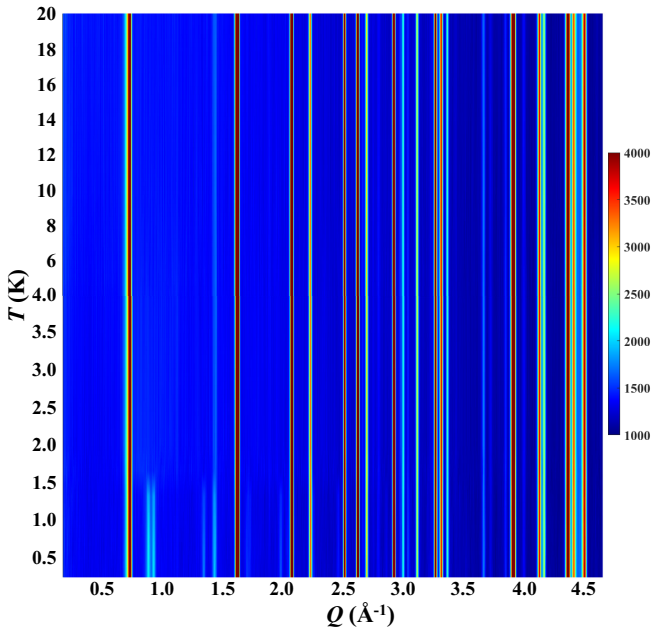

FIG. 2. Contour plot of the neutron powder-diffraction pattern of the $RbFe(SeO_4)_2$ sample over a temperature range from 0.25 to 20 K. The vertical axis represents temperature, while the horizontal axis corresponds to the momentum transfer Q of the scattered neutrons. The color scale on the right indicates intensity, with red representing the highest intensity and blue the lowest.

where two sharp peaks appear at 1 and 3.2 T. At 3.68 K, in the paramagnetic phase, both peaks disappear in the *dM/dH* curve. The magnetization plateau in the *M-H* curve and the peaks in the *dM/dH* curve are characteristic features of frustrated 2D triangular antiferromagnetic systems.

To determine the magnetic structure below T_N, we performed neutron powder-diffraction experiments on crushed $RbFe(SeO_4)_2$ single crystals. These measurements were carried out over a temperature range of 20 to 0.25 K using the HB-2A neutron powder diffractometer at the High Flux Isotope Reactor (HFIR), Oak Ridge National Laboratory (ORNL), with a constant neutron wavelength of 2.41 Å [24]. Figure 2 presents a contour map of the neutron-diffraction intensity, where the vertical axis represents temperature and the horizontal axis represents the momentum transfer of the scattered neutrons. Red corresponds to the highest intensity, while blue indicates the lowest. As shown in Fig. 2, no signs of a structural phase transition are observed above 1.6 K. However, a set of incommensurate magnetic peaks ($Q \sim 0.9$ Å^{-1}) emerges near 1.6 K, consistent with the T_N identified from the χ-T measurements.

We performed Rietveld refinement on the neutron diffraction data. Figure 3(a) shows the refinement results at 20 K. The black crosses represent the measured neutron intensities, while the red solid line corresponds to the calculated pattern based on our structural model. The green vertical ticks indicate the Bragg-peak positions of the $RbFe(SeO_4)_2$ phase, and the magenta ticks mark the Al peaks originating from the sample holder. The primary phase of the sample is

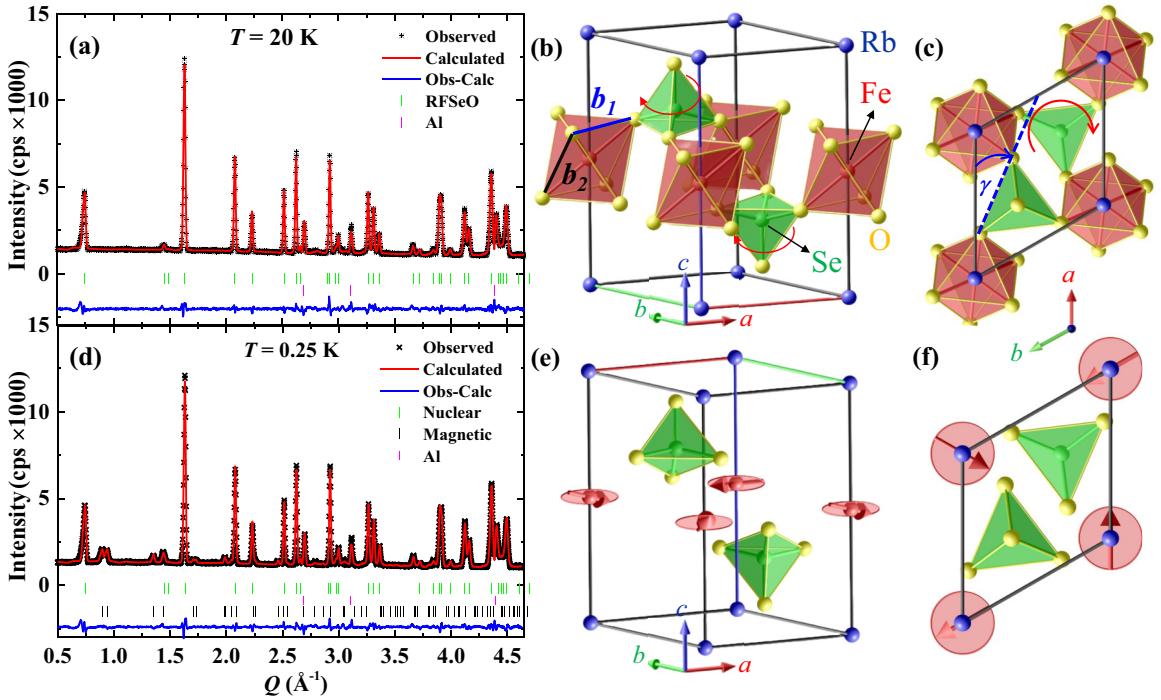

FIG. 3. (a) Neutron diffraction pattern measured at 20 K, along with the refinement of the pattern. (b), (c) Refined $P\bar{3}$ lattice structure of RFSeO at 20 K. The red circular arrows indicate the ferrorotational motion of the SeO_4 polyhedra. γ denotes the ferrorotational angle extracted from the refinement. b_1 and b_2 represent two distinct O-O band lengths within the FeO_6 octahedra. (d) Neutron diffraction pattern measured at 0.25 K, with the refinement of the magnetic peaks using the Γ_2 irreducible representation. (e), (f) Magnetic structure corresponding to the Γ_2 representation.

TABLE I. Structural parameters for $P\bar{3}$ space group at 20 K. The refined lattice parameters are $a = 4.9947(3)$ Å and $c = 8.4440(1)$ Å. The goodness of fit $\chi^2 \sim 5.113$ and $R_{wp} \sim 10.7$.

Atoms	x	y	z	Occ	B (Å^2)	Wyckoff symbol
Rb	0	0	0	0.9114(1)	0.22913	1a
Fe	0	0	1/2	0.9087(7)	0.00001	1b
Se	2/3	1/3	0.2895(4)	0.9356(5)	0.56503	2d
O1	0.9621(7)	0.6747(8)	0.3546(6)	0.9218(6)	0.20821	6g
O2	2/3	1/3	0.1044(5)	1.0000(0)	0.00001	2d

well described by the ferrorotational space group $P\bar{3}$, which shows good agreement with the experimental data, yielding an overall goodness of fit $\chi^2 \sim 5.113$ and $R_{wp} \sim 10.7$. Figures 3(b) and 3(c) illustrate the refined $P\bar{3}$ crystal structure. The structure consists of alternating layers of SeO_4 tetrahedra, FeO_6 octahedra, and Rb ions. The SeO_4 tetrahedra exhibit clockwise (or counterclockwise) rotations around the c axis, as indicated by the red arrows in Fig. 3(b), giving rise to the ferrorotational order with a rotation angle $\gamma \sim 23°$. The magnetic Fe^{3+} ions are separated by SeO_4 tetrahedra and form a 2D triangular layered structure, as shown in Figs. 3(e) and 3(f). The refined structural parameters are summarized in Table I. The occupancy of O(2) is 1.0, indicating that the vacancies at this site are negligible. The occupancies of all other ions are slightly below 1.0, suggesting the presence of vacancies *at* their respective sites. Moreover, the refinement remained stable and produced the most physically reasonable results only when the B factors of Fe and O(2) were fixed at a very small value (0.00001).

Figure 3(d) presents the neutron diffraction data collected at 0.25 K, corresponding to the magnetically ordered phase. In addition to the primary $P\bar{3}$ nuclear structure, a set of incommensurate magnetic peaks is observed (highlighted by the black vertical lines). All magnetic peaks can be indexed with a single propagation vector $k = (1/3, 1/3, 0.428)$. A representational analysis was performed using the SARAh program to determine the symmetry-allowed magnetic structures [25–27]. The magnetic representation of the Fe site is expressed as a sum of irreducible representations (IRs) of G_k:

$$\Gamma_{\text{Mag}} = \sum_{\nu} n_\nu \Gamma_\nu^\mu,$$

where n_ν is the number of times that the IR Γ_ν of order μ appears in the magnetic representation Γ_{Mag} for the chosen crystallographic site. The decomposition of Γ_{Mag} into the nonzero IRs of G_k for the magnetic Fe site, along with their associated basis vectors ψ_n, is summarized in Table II. The labeling of the propagation vector and the IRs follows the scheme used by Kovalev [28]. For the given propagation vector and the crystal symmetry of $RbFe(SeO_4)_2$, only three IRs are allowed: Γ_1, Γ_2, and Γ_3. Γ_1 corresponds to a spin-density wave with magnetic moments aligned along the c axis and is achiral. Γ_2 and Γ_3 describe left-handed and right-handed chiral helical magnetic structures, respectively. Since the magnetic ground state of the isostructural compound $RbFe(SO_4)_2$ is known to be a chiral helical structure, it is highly plausible that $RbFe(SeO_4)_2$ adopts a similar ground state [20,21]. Based on this reasoning, we refined the magnetic structure using the Γ_2 chiral helical model. The refinement results are shown in Fig. 3(d) and exhibit good agreement with the experimental data, yielding a $\chi^2 \sim 9.69$ and $R_{wp} \sim 9.93$. The refined structure features a 120° spin arrangement within each triangular layer and a chiral helical twist along the c axis between adjacent layers, as illustrated in Figs. 3(e) and 3(f). The refined magnetic moment for the Fe^{3+} ion in $RbFe(SeO_4)_2$ is 4.042 μ_B, which is slightly smaller than the expected spin-only value of 5.0 μ_B ($S = 5/2$, $g \sim 2$). This reduction is likely due to strong magnetic fluctuations arising from geometric frustration and low-dimensional interactions inherent to the triangular lattice of $RbFe(SeO_4)_2$. Similar fluctuation-induced reductions of ordered magnetic moments have been reported in $SrCuTe_2O_6$, $KFe_3(OH)_6(SO_4)_2$, $Cs_2Cu_3SnF_{12}$, $Na_3Fe(PO_4)_2$, $Ba_3MnNb_2O_9$, and $Ba_8MnNb_6O_{24}$ [29–34]. In particular, $Na_3Fe(PO_4)_2$ (Fe^{3+}), $Ba_3MnNb_2O_9$ (Mn^{2+}), and $Ba_8MnNb_6O_{24}$ (Mn^{2+}) are all $S = 5/2$ triangular-layered quasi-two-dimensional systems with strong frustration, closely analogous to $RbFe(SeO_4)_2$. The ordered moments are reported as 4.7 μ_B for $Ba_3MnNb_2O_9$, 4.1 μ_B for $Ba_8MnNb_6O_{24}$, and 1.52 μ_B for $Na_3Fe(PO_4)_2$.

To quantitatively understand the magnetic phase transition, we measured the intensity of the magnetic peak at (1/3, 1/3, 0.428)—i.e., the order parameter—as a function of temperature, as shown in Fig. 4(a). The intensity curve was fitted to a power law $I \propto (T_N - T)^{2\beta}$ over a narrow temperature range below T_N. The fit yields $T_N \sim 1.62$ K, which is in

TABLE II. Basis vectors for the space group $P\bar{3}$ with $k \sim (1/3, 1/3, 0.428)$. The decomposition of the magnetic representation for the Fe site (0, 0, 0.5) is $\Gamma_{\text{Mag}} = 1\Gamma_1^1 + 1\Gamma_2^1 + 1\Gamma_3^1$.

			BV components					
IR	BV	Atom	$m \parallel a$	$m \parallel b$	$m \parallel c$	$im \parallel a$	$im \parallel b$	$im \parallel c$
Γ_1	ψ_1	Fe	0	0	3	0	0	0
Γ_2	ψ_2	Fe	1.5	0	0	−0.866	−1.732	0
Γ_3	ψ_3	Fe	1.5	0	0	−0.866	−1.732	0

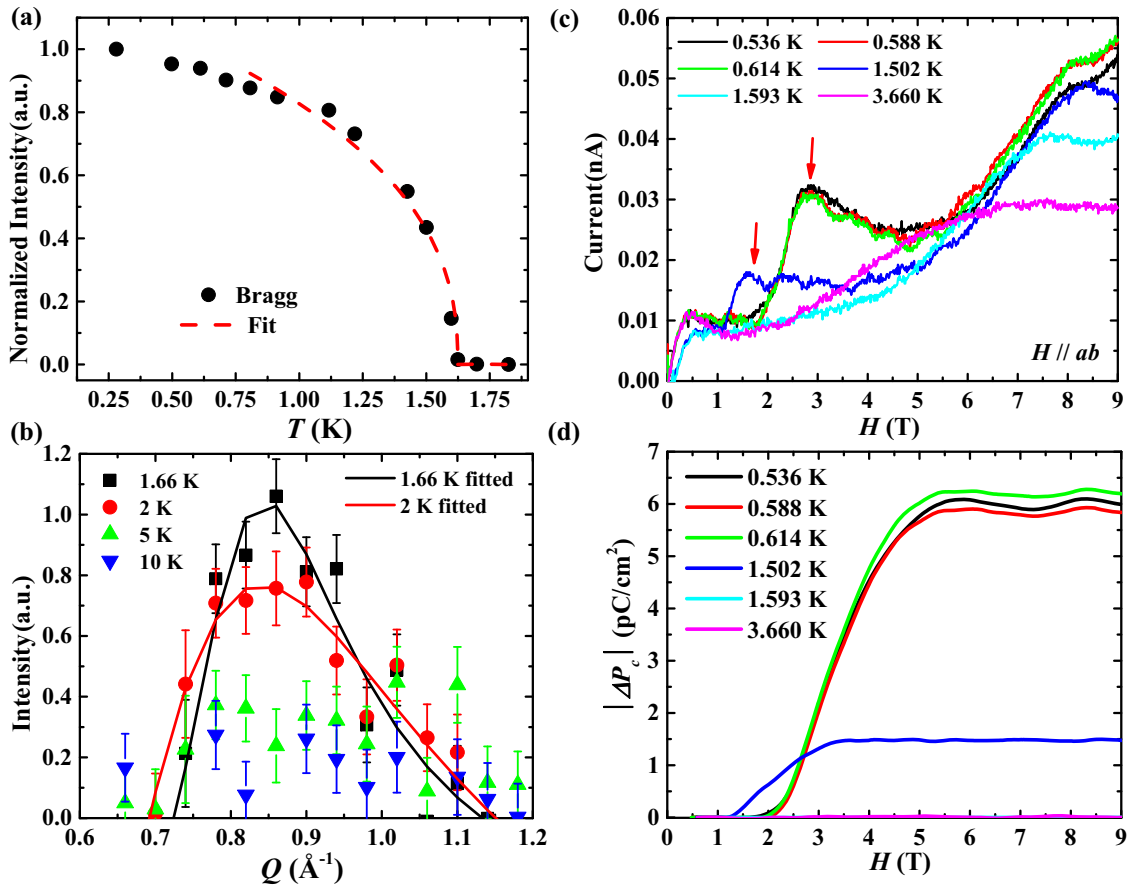

FIG. 4. (a) The temperature dependence of the intensity of the magnetic peak at (1/3, 1/3, 0.428). The dashed red line indicates the fit. (b) Magnetic diffuse-scattering intensities for 1.66, 2, 5, and 10 K. Solid lines represent the fitted curves. (c) The magnetoelectric current was measured as a function of magnetic field (H // ab) at various temperatures. (d) Field dependence of the calculated change in ferroelectric polarization, $|\Delta P_c|$-H.

agreement with the value determined from the χ-T measurements, and $\beta \sim 0.204$, which is close to the effective critical exponent expected for the 2D XY model [35]. This result is consistent with the in-plane anisotropy and the 2D nature of the $RbFe(SeO_4)_2$. The high frustration ratio ($-\theta_{CW}/T_N \sim 5.87$) and the 2D XY signature suggest the presence of short-range magnetic correlations even above T_N in $RbFe(SeO_4)_2$. To investigate this possibility, we performed background subtraction and rebinning of the neutron diffraction patterns measured at 1.66, 2, 5, and 10 K, using the 20 K data as the high-temperature reference. The results are presented in Fig. 4(b). As shown in Fig. 4(b), diffuse-scattering intensity begins to emerge below 5 K and becomes more pronounced at 2 and 1.66 K. This diffuse scattering is also evident in the raw data, as displayed in Fig. S1 of the Supplemental Material [36]. The 1.66 and 2 K diffuse scattering data shown in Fig. 4(b) were fitted using a phenomenological asymmetric Lorentzian function

$$I \propto \frac{\xi}{\pi} \cdot \frac{1 + \alpha((q - q_0))}{1 + ((q - q_0)\xi)^2},$$

where α is the asymmetry parameter, q is the wave vector, and ξ is the magnetic correlation length. The extracted correlation lengths are $\xi = 3.94$ Å for K and $\xi = 7.53$ Å for 1.66 K.

In the magnetically ordered state, the chiral helical magnetic structure of $RbFe(SeO_4)_2$ may interact with the structural ferrorotational order, potentially giving rise to multiferroic and magnetoelectric properties along the c axis, as previously observed in the isostructural compound $RbFe(SO_4)_2$ [20,21]. To investigate this possibility, we measured the c-axis magnetoelectric coupling as a function of the magnetic field (H // ab) at various temperatures using the magnetoelectric current method. The measurements were carried out at the pulsed magnet facility at Los Alamos National Laboratory (LANL). A He^3 insert was used to reach the base temperature of approximately 0.5 K. As shown in the current vs magnetic-field curves in Fig. 4(c), only a broad background signal is observed above 1.593 K. At 1.502 K, a distinct current peak emerges in the range of 1 to 3 T, suggesting the onset of magnetoelectric coupling effect, i.e., the magnetic-field-induced change in ferroelectric polarization. As the temperature decreases, this current peak becomes more pronounced and shifts toward higher magnetic fields. We subtracted the background and integrated the current to extract the magnetic-field-induced change in ferroelectric polarization, $|\Delta P_c|$, as shown in Fig. 4(d). The results reveal that this change occurs in the magnetically ordered phase of $RbFe(SeO_4)_2$. Furthermore, the transition

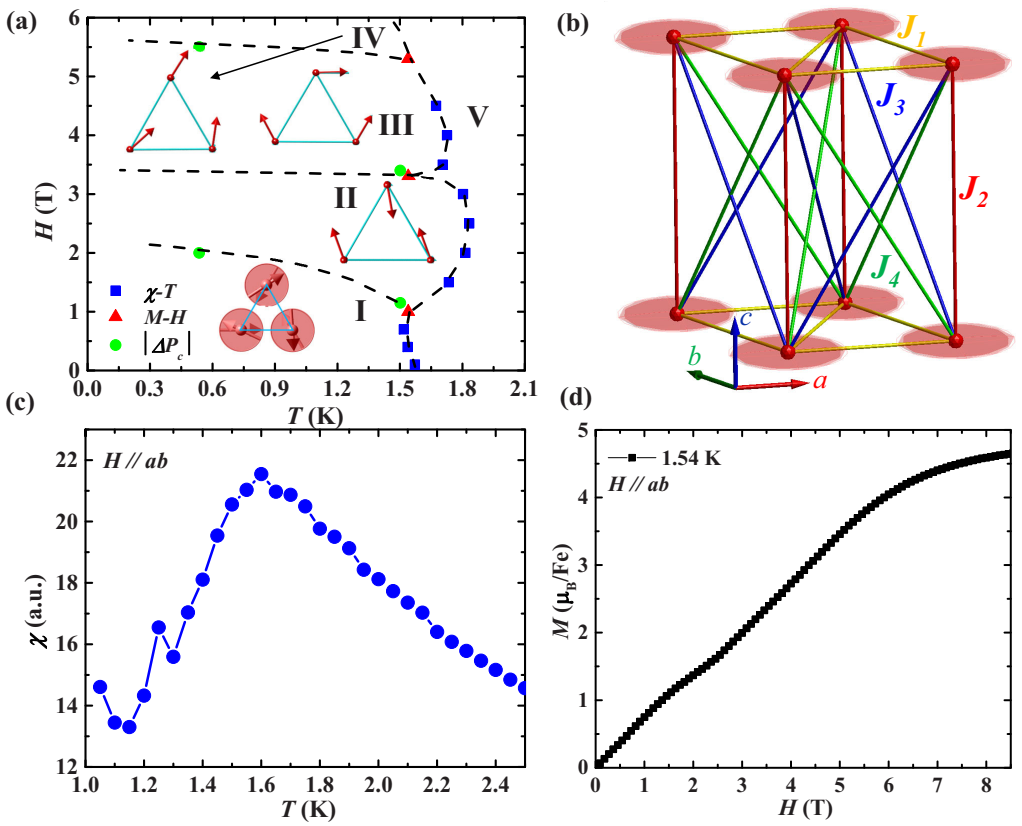

FIG. 5. (a) The *H*-*T* phase diagram constructed from the $|\Delta P_c|$-*H*, χ-*T*, and *M*-*H* curves. The insets illustrate the simulated magnetic structures corresponding to different regions of the phase diagram. (b) Exchange-interaction paths in the $RbFe(SeO_4)_2$. (c) Simulated χ-*T* curve obtained from Monte Carlo calculations. (d) Simulated *M*-*H* curve obtained from Monte Carlo calculations.

magnetic field of $|\Delta P_c|$ at 1.502 K closely matches that of the *M*-*H* curve at 1.54 K [Fig. 1(c)], suggesting that the magnetoelectric coupling effect in $RbFe(SeO_4)_2$ is linked to the magnetic-field-induced changes in the magnetic structures. Our magnetoelectric-current method does not allow the determination of the absolute value of the polarization P_c; therefore, it is not rigorous to claim that $RbFe(SeO_4)_2$ is ferroelectric below T_N. However, our previous pyrocurrent measurements under various magnetic fields on an isostructural $RbFe(SO_4)_2$ confirmed that $RbFe(SO_4)_2$ is ferroelectric in the chiral helical magnetic phase ($T < T_N \sim 4$ K) at low magnetic fields, and becomes nonferroelectric in the achiral magnetic phase at higher magnetic fields [15,16,20,21]. A similar magnetic-field-induced change in ferroelectric polarization was also observed in $RbFe(SO_4)_2$. Thus, it is reasonable to deduce that $RbFe(SeO_4)_2$ is likewise ferroelectric in the chiral helical magnetic phase at low magnetic fields below $T_N \sim 1.62$ K.

To further illustrate the relationship between ferroelectricity, magnetic structure, temperature, and magnetic field, we constructed the *H*-*T* phase diagram shown in Fig. 5(a), based on the results from the $|\Delta P_c|$-*H* data, χ-*T* measurements, and *M*-*H* curves. Five distinct regions are clearly identified. At high temperatures ($T > 1.9$ K), the system resides in the paramagnetic and paraelectric phase (V). At low magnetic fields ($H < 2$ T) and low temperatures ($T < 1.6$ K), the system enters the chiral helical magnetic and ferroelectric phase (I). The ferroelectric polarization arises due to a key permutable symmetry operational similarity (SOS) relationship, expressed as $\boldsymbol{a} \bullet \mathcal{C} = \mathcal{P}$ [37]. Here, $\boldsymbol{a}$ represents the ferrorotational vector, $\mathcal{C}$ denotes chirality, and $\mathcal{P}$ corresponds to electric polarization. This relationship suggests that if the magnetic structure loses its chirality, the ferroelectricity could be suppressed. Therefore, the magnetic structures of phases II, III, and IV shown in Fig. 5(a) are expected to be achiral.

The possible magnetic structures of phases II, III, and IV are further determined by our Monte Carlo simulations using the following spin Hamiltonian:

$$\mathcal{H} = J_1 \sum_{\langle i,j \rangle} \vec{S}_{i,p} \cdot \vec{S}_{j,p} + \sum_i J_2 \vec{S}_{i,p} \cdot \vec{S}_{i,p+1} + \sum_{\langle\langle i,j,k \rangle\rangle} (J_3 \vec{S}_{i,p} \cdot \vec{S}_{j,p+1} + J_4 \vec{S}_{i,p} \cdot \vec{S}_{k,p+1}) + D \sum_i S^z_{i,p} S^z_{i,p} - g\mu_B \vec{H} \cdot \sum_i \vec{S}_{i,p}.$$

As illustrated in Fig. 5(b), $J_1 > 0$ is the intraplane nearest-neighbor coupling constant (yellow bonds), and J_2 represents the interplane nearest-neighbor coupling (red bonds). J_3 (blue bonds) and J_4 (green bonds) denote two distinct next-nearest-neighbor interplane coupling constants. $D > 0$ is the single-ion anisotropy constant, and $\vec{H}$ is the external magnetic field. The index p labels the lattice plane, while i, j, and k indicate sites on the triangular lattice. The $\langle \ldots \rangle$

TABLE III. Comparison of bond lengths in the lattice structures of $RbFe(SeO_4)_2$ (20 K) and $RbFe(SO_4)_2$ (100 K) [20,21]. Fe-Fe (*ab*) denotes the nearest Fe-Fe bond in the *ab* plane (intralayer), and Fe-Fe (*c*) is the nearest Fe-Fe bond along the *c* axis (interlayer). The O-O (b_1) and O-O (b_2) bonds are defined in Fig. 3(b). The unit for all bond lengths is Å.

	Se/S-O	Fe-Fe (*ab*)	Fe-Fe (*c*)	Fe-O	O-O (b_1)	O-O (b_2)
$RbFe(SeO_4)_2$	1.6948	4.9947	8.4440	1.9681	2.6650	2.8969
$RbFe(SO_4)_2$	1.4839	4.8404	8.2390	1.9925	2.7666	2.8682

notation denotes summation over nearest neighbors, and $\langle\langle \ldots \rangle\rangle$ refers to summation over interplane next-nearest neighbors. Notably, the ferrorotational order in $RbFe(SeO_4)_2$ breaks mirror-reflection symmetries in the *ab* plane, resulting in nonequivalent super-superexchange interactions J_3 and J_4 [16,21]. These nonequivalent J_3 and J_4 terms introduce a relative twist between adjacent layers, which ultimately gives rise to the chiral helical magnetic structure. We estimate the value of J_1 to be approximately 0.037 meV, which is close to the effective exchange-coupling constant of 0.045 meV derived from fitting the Curie-Weiss temperature. For our simulations, we used the following parameters: $J_2 \sim 0.001$ meV, $J_3 \sim 0.0001$ meV, and $J_4 \sim 0.0002$ meV. A small single-ion anisotropy $D \sim 0.001$ meV was included to preserve the in-plane anisotropy of the magnetic structure. By minimizing the magnetic energy, we optimized the magnetic structure of $RbFe(SeO_4)_2$ in the absence of an external magnetic field. The resulting ground state is a chiral helical structure with a propagation vector of (1/3, 1/3, 0.4298), which closely matches the neutron diffraction results at 0.25 K. This agreement confirms the reasonableness of the exchange-coupling parameters adopted in our model.

Using our Monte Carlo simulation model, we also optimized the magnetic structures of phases II, III, and IV under a magnetic field of 2.5, 5, and 7 T along the *a* axis, respectively, below the magnetic-ordering temperature. The optimized magnetic structures are displayed in the inset of Fig. 5(a) for each of these phases. Between 2 and 3 T, and below 1.82 K, the optimized magnetic structure corresponds to a collinear ferrimagnetic phase (II), with spins closely aligned along the *a* axis. Between 3.5 and 5.5 T, and below 1.75 K, the optimized structure is noncollinear ferrimagnetic (III) with a larger net moment along the *a* axis. At higher fields ($H >$ 5.5 T) and temperatures below 1.6 K, the optimized structure corresponds to a noncollinear ferrimagnetic phase (IV) with an even larger net magnetic moment. All three phases II, III, and IV are achiral and therefore likely paraelectric, consistent with the SOS relationship.

Furthermore, we performed Monte Carlo simulations using the Metropolis-Hastings algorithm to compute the χ-T curve [38]. The calculated results, shown in the inset of Fig. 5(c), display a clear peak near 1.6 K, consistent with the experimental data in Fig. 1(b). We also simulated the *M*-*H* curve at 1.54 K. As shown in Fig. 5(d), the simulated *M*-*H* curve also exhibits a 1/3 magnetization plateau between 1 and 3 T, in good agreement with the experimental results in Fig. 1(c). This consistency further validates the exchange-coupling constants used in our model.

All the estimated exchange-coupling constant—J_1, J_2, J_3, J_4, and D—for $RbFe(SeO_4)_2$ are smaller than those of the isostructural compound $RbFe(SO_4)_2$, which has reported values of $J_1 \sim 0.086$ meV, $J_2 \sim 0.005$ meV, $J_3 \sim 0.001$ meV, $J_4 \sim 0.00128$ meV, and $D \sim 0.027$ meV [20]. This marked difference likely originates from the larger size of the SeO_4 groups (which also feature longer Se-O bonds) and the resulting lattice distortions they introduce. To examine this hypothesis, we compare key structural parameters—Fe-Fe, Fe-O, Se/S-O bond lengths, and two O-O distances [b_1 and b_2, as defined in Fig. 3(b)] within the FeO_6 octahedra—for both $RbFe(SeO_4)_2$ and $RbFe(SO_4)_2$ in Table III. Since FeO_6 octahedra are spatially separated by SeO_4 tetrahedra, the larger size of SeO_4 can significantly increase both the intralayer and interlayer Fe-Fe distances, as shown in Table III, thereby reducing the strengths of both J_1 and J_2 in $RbFe(SeO_4)_2$. Moreover, $RbFe(SeO_4)_2$ exhibits shorter Fe-O bond lengths within the FeO_6 octahedra, suggesting that these octahedra are more isolated compared to those in $RbFe(SO_4)_2$, which further contributes to the weakening of magnetic-exchange interactions.

III. CONCLUSIONS

In conclusion, this study presents a comprehensive investigation of the structural, magnetic, and phase-transition properties of $RbFe(SeO_4)_2$, a ferrorotational material that exhibits significant magnetic frustration and a chiral helical magnetic structure below 1.6 K. Neutron powder diffraction confirms the ferrorotational $P\bar{3}$ lattice symmetry and reveals the emergence of incommensurate magnetic peaks associated with a chiral helical magnetic ground state. The interplay between ferrorotational order and magnetic chirality gives rise to magnetoelectric coupling in $RbFe(SeO_4)_2$, as confirmed by magnetoelectric current data. Neutron scattering also reveals diffuse scattering above T_N, indicating the presence of short-range magnetic correlations above the magnetic-ordering temperature. A rich *H*-*T* phase diagram is constructed based on magnetoelectric coupling data, magnetic susceptibility, and magnetization data, identifying multiple magnetic phases. Monte Carlo simulations were used to determine the magnetic exchange-coupling constants and field-dependent magnetic structures, successfully reproducing the experimental *M*-*H* and χ-T curves. The exceptionally low T_N and weak magnetic exchange interactions are attributed to the large size of the SeO_4 tetrahedra, which increases Fe-Fe distances and reduces superexchange pathways.

In the context of frustrated magnets, understanding how spin magnitude, dimensionality, and frustration influence the crossover between classical and quantum magnetic regimes remains an important challenge. $RbFe(SeO_4)_2$, with its large spin ($S = 5/2$), strong frustration, and extremely low ordering temperature, provides a promising platform for such studies. Furthermore, materials with large spin and low ordering

temperatures have potential applications in adiabatic demagnetization refrigeration. $RbFe(SeO_4)_2$, composed of abundant and inexpensive elements, could serve as a viable alternative to rare-earth-based paramagnetic salts currently used in adiabatic demagnetization refrigeration. Our fundamental characterization of $RbFe(SeO_4)_2$ not only reveals intriguing physics but may also stimulate further research into its functional applications.

IV. EXPERIMENTAL SECTION

Single crystals of $RbFe(SO_4)_2$ were synthesized using the hydrothermal method in a 50-ml Teflon-lined autoclave at 483 K. The χ-T and M-H curves were measured using a 9-T Cryogen Free Measurement System (Cryogenic Limited). The magnetoelectric coupling was measured by the magnetoelectric current method with an SR570 low-noise current preamplifier at the pulsed-magnet facility at LANL. Neutron diffraction experiments were conducted at the HB-2A powder diffractometer at the HFIR at ORNL. A He^3 insert was utilized to achieve a base temperature of 0.25 K, and a Ge(113) monochromator provided a constant neutron wavelength of 2.41 Å. The neutron data refinements were performed using the FullProf and SARAh packages [27,39]. The optimization of the magnetic structures and the Monte Carlo simulation were performed using the SpinW package [38].

ACKNOWLEDGMENTS

J.Y. acknowledges support by the DOE under Grant No. DOE: DE-SC0021188. This research used resources at the High Flux Isotope Reactor, a DOE Office of Science User Facility operated by the Oak Ridge National Laboratory. Part of this work was performed at the National High Magnetic Field Laboratory, which is supported by the National Science Foundation Cooperative Agreement No. DMR-2128556 and the State of Florida and the U.S. Department of Energy.

DATA AVAILABILITY

The data that support the findings of this article are not publicly available. The data are available from the authors upon reasonable request.

[1] S. T. Bramwell and M. J. P. Gingras, Spin ice state in frustrated magnetic pyrochlore materials, Science **294**, 1495 (2001).

[2] T. H. Han, J. S. Helton, S. Chu, D. G. Nocera, J. A. Rodriguez-Rivera, C. Broholm, and Y. S. Lee, Fractionalized excitations in the spin-liquid state of a kagome-lattice antiferromagnet, Nature (London) **492**, 406 (2012).

[3] L. Balents, Spin liquids in frustrated magnets, Nature (London) **464**, 199 (2010).

[4] C. Broholm, R. J. Cava, S. A. Kivelson, D. G. Nocera, M. R. Norman, and T. Senthil, Quantum spin liquids, Science **367**, eaay0668 (2020).

[5] Y. Zhou, K. Kanoda, and T. K. Ng, Quantum spin liquid states, Rev. Mod. Phys. **89**, 025003 (2017).

[6] J. Yang, A. Samarakoon, S. Dissanayake, H. Ueda, I. Klich, K. Iida, D. Pajerowski, N. P. Butch, Q. Huang, J. R. D. Copley, and S. H. Lee, Spin jam induced by quantum fluctuations in a frustrated magnet, Proc. Nat. Acad. Sci. USA **112**, 11519 (2015).

[7] T. Kurumaji, T. Nakajima, M. Hirschberger, A. Kikkawa, Y. Yamasaki, H. Sagayama, H. Nakao, Y. Taguchi, T. H. Arima, and Y. Tokura, Skyrmion lattice with a giant topological Hall effect in a frustrated triangular-lattice magnet, Science **365**, 914 (2019).

[8] F. Yokaichiya, A. Krimmel, V. Tsurkan, I. Margiolaki, P. Thompson, H. N. Bordallo, A. Buchsteiner, N. Stüßer, D. N. Argyriou, and A. Loidl, Spin-driven phase transitions in $ZnCr_2Se_4$ and $ZnCr_2S_4$ probed by high-resolution synchrotron x-ray and neutron powder diffraction, Phys. Rev. B **79**, 064423 (2009).

[9] R. Coldea, D. A. Tennant, R. A. Cowley, D. F. McMorrow, B. Dorner, and Z. Tylczynski, Neutron scattering study of the magnetic structure of Cs_2CuCl_4, J. Phys.: Condens. Matter **8**, 7473 (1996).

[10] H. Serrano-González, S. T. Bramwell, K. D. M. Harris, B. M. Kariuki, L. Nixon, I. P. Parkin, and C. Ritter, Magnetic structures of the triangular lattice magnets $AFe(SO_4)_2$ (A = K, Rb, Cs), J. Appl. Phys. **83**, 6314 (1998).

[11] H. Serrano-González, S. T. Bramwell, K. D. M. Harris, B. M. Kariuki, L. Nixon, I. P. Parkin, and C. Ritter, Structural and magnetic characterization of the frustrated triangular-lattice antiferromagnets $CsFe(SO_4)_2$ and $RbFe(SO_4)_2$, Phys. Rev. B **59**, 14451 (1999).

[12] G. R. Blake, L. C. Chapon, P. G. Radaelli, S. Park, N. Hur, S. W. Cheong, and J. Rodríguez-Carvajal, Spin structure and magnetic frustration in multiferroic RMn_2O_5 (R = Tb, Ho, Dy), Phys. Rev. B **71**, 214402 (2005).

[13] T. Inami, Neutron powder diffraction experiments on the layered triangular-lattice antiferromagnets $RbFe(MoO_4)_2$ and $CsFe(SO_4)_2$, J. Solid State Chem. **180**, 2075 (2007).

[14] A. J. Hearmon, F. Fabrizi, L. C. Chapon, R. D. Johnson, D. Prabhakaran, S. V. Streltsov, P. J. Brown, and P. G. Radaelli, Electric field control of the magnetic chiralities in ferroaxial multiferroic $RbFe(MoO_4)_2$, Phys. Rev. Lett. **108**, 237201 (2012).

[15] J. S. White, C. Niedermayer, G. Gasparovic, C. Broholm, J. M. S. Park, A. Y. Shapiro, L. A. Demianets, and M. Kenzelmann, Multiferroicity in the generic easy-plane triangular lattice antiferromagnet $RbFe(MoO_4)_2$, Phys. Rev. B **88**, 060409(R) (2013).

[16] K. Cao, R. D. Johnson, F. Giustino, P. G. Radaelli, G. C. Guo, and L. He, First-principles study of multiferroic $RbFe(MoO_4)_2$, Phys. Rev. B **90**, 024402 (2014).

[17] Y. Li, G. Chen, W. Tong, L. Pi, J. Liu, Z. Yang, X. Wang, and Q. Zhang, Rare-earth triangular lattice spin liquid: A single-crystal study of $YbMgGaO_4$, Phys. Rev. Lett. **115**, 167203 (2015).

[18] Y. Shen, Y. D. Li, H. C. Walker, P. Steffens, M. Boehm, X. Zhang, S. Shen, H. Wo, G. Chen, and J. Zhao, Fractionalized excitations in the partially magnetized spin liquid candidate $YbMgGaO_4$, Nat. Commun. **9**, 4138 (2018).

[19] J. A. M. Paddison, M. Daum, Z. Dun, G. Ehlers, Y. Liu, M. B. Stone, H. Zhou, and M. Mourigal, Continuous excitations of the triangular-lattice quantum spin liquid $YbMgGaO_4$, Nat. Phys. **13**, 117 (2017).

[20] J. Yang, D. Obeysekera, W. Ratcliff, L. Li, S. N. Neal, J. L. Musfeldt, and S. Yano, Multiferroicity and phase diagram of ferro-rotational magnet $RbFe(SO_4)_2$, J. Phys.: Condens. Matter **37**, 175701 (2025).

[21] J. Yang, T. Tyson, J. Young, W. Ratcliff, Y. Gao, D. Obeysekera, X. Guo, R. Owen, L. Zhao, and S.-w. Cheong, Electric-field manipulation of magnetic chirality in a homo-ferro-rotational helimagnet, Adv. Sci. **11**, 2402048 (2024).

[22] B. G. Bazarov, T. V. Namsaraeva, R. F. Klevtsova, A. G. Anshits, T. A. Vereshchagina, L. A. Glinskaya, K. N. Fedorov, and Zh. G. Bazarova, Growth and crystal structure of binary molybdate $CsFe(MoO_4)_2$, Crystallogr. Rep. **55**, 591 (2010).

[23] S. A. Klimin, M. N. Popova, B. N. Mavrin, P. H. M. van Loosdrecht, L. E. Svistov, A. I. Smirnov, L. A. Prozorova, H.-A. K. von Nidda, Z. Seidov, A. Loidl, A. Y. Shapiro, and L. N. Demianets, Structural phase transition in the two-dimensional triangular lattice antiferromagnet $RbFe(MoO_4)_2$, Phys. Rev. B **68**, 174408 (2003).

[24] S. Calder, K. An, R. Boehler, C. R. Dela Cruz, M. D. Frontzek, M. Guthrie, B. Haberl, A. Huq, S. A. J. Kimber, J. Liu, J. J. Molaison, J. Neuefeind, K. Page, A. M. dos Santos, K. M. Taddei, C. Tulk, and M. G. Tucker, A suite-level review of the neutron powder diffraction instruments at Oak Ridge National Laboratory, Rev. Sci. Instrum. **89**, 092701 (2018).

[25] E. F. Bertaut, Representation analysis of magnetic structures, Acta Crystallogr. Sect. A **24**, 217 (1968).

[26] E. F. Bertaut, On group theoretical techniques in magnetic structure analysis, J. Magn. Magn. Mater. **24**, 267 (1981).

[27] A. S. Wills, New protocol for the determination of magnetic structures using simulated annealing and representational analysis (SARAh), Physica B **276**, 680 (2000).

[28] O. V. Kovalev, *Irreducible Representations of the Space Groups* (Gordon and Breach Science Publishers Inc., New York, 1965).

[29] S. J. Sebastian, S. S. Islam, A. Jain, S. M. Yusuf, M. Uhlarz, and R. Nath, Collinear order in the spin-5/2 triangular-lattice antiferromagnet $Na_3Fe(PO_4)_2$, Phys. Rev. B **105**, 104425 (2022).

[30] K. Matan, T. Ono, G. Gitgeatpong, K. de Roos, P. Miao, S. Torii, T. Kamiyama, A. Miyata, A. Matsuo, K. Kindo, S. Takeyama, Y. Nambu, P. Piyawongwatthana, T. J. Sato, and H. Tanaka, Magnetic structure and high-field magnetization of the distorted kagome lattice antiferromagnet $Cs_2Cu_3SnF_{12}$, Phys. Rev. B **99**, 224404 (2019).

[31] T. Inami, M. Nishiyama, S. Maegawa, and Y. Oka, Magnetic structure of the kagome lattice antiferromagnet potassium jarosite $KFe_3(OH)_6(SO_4)_2$, Phys. Rev. B **61**, 12181 (2000).

[32] P. Saeaun, Y. Zhao, P. Piyawongwatthana, T. J. Sato, F. C. Chou, M. Avdeev, G. Gitgeatpong, and K. Matan, Magnetic properties and magnetic structure of the frustrated quasi-one-dimensional antiferromagnet $SrCuTe_2O_6$, Phys. Rev. B **102**, 134407 (2020).

[33] R. Rawl, L. Ge, Z. Lu, Z. Evenson, C. R. Dela Cruz, Q. Huang, M. Lee, E. S. Choi, M. Mourigal, H. D. Zhou, and J. Ma, $Ba_8MnNb_6O_{24}$: A model two-dimensional spin-5/2 triangular lattice antiferromagnet, Phys. Rev. Mater. **3**, 054412 (2019).

[34] M. Lee, E. S. Choi, X. Huang, J. Ma, C. R. Dela Cruz, M. Matsuda, W. Tian, Z. L. Dun, S. Dong, and H. D. Zhou, Magnetic phase diagram and multiferroicity of $Ba_3MnNb_2O_9$: A spin-5/2 triangular lattice antiferromagnet with weak easy-axis anisotropy, Phys. Rev. B **90**, 224402 (2014).

[35] R. Gupta and C. F. Baillie, Critical behavior of the two-dimensional XY model, Phys. Rev. B **45**, 2883 (1992).

[36] See Supplemental Material at http://link.aps.org/supplemental/10.1103/wjq7-tlk7 for the neutron diffraction patterns in the range from 0.6 to 1.2 Å were measured at 20 K, 10 K, 5 K, 2 K, and 1.66 K. The diffuse-scattering intensity emerges between 0.75 and 0.95 Å below 5 K and becomes pronounced at 2 K and 1.66 K.

[37] S. W. Cheong, S. Lim, K. Du, and F.-T. Huang, Permutable SOS (symmetry operational similarity), npj Quantum Mater. **6**, 58 (2021).

[38] S. Toth and B. Lake, Linear spin wave theory for single-Q incommensurate magnetic structures, J. Phys.: Condens. Matter **27**, 166002 (2015).

[39] J. Rodriguez-Carvajal, Recent advances in magnetic structure determination by neutron powder diffraction, Physica B **192**, 55 (1993).